Exploring plasmonic hotspots of Au tilted nanocolumns and their application to the uracil detection by surface-enhanced Raman scattering

Grégory Barbillon, Mathilde Faure, Ludovic Douillard, Eric Caudron, Christophe Humbert, José Miguel García-Martín

Graphical Abstract

Exploring plasmonic hotspots of Au tilted nanocolumns and their application to the uracil detection by surface-enhanced Raman scattering

Grégory Barbillon, Mathilde Faure, Ludovic Douillard, Eric Caudron, Christophe Humbert, José Miguel García-Martín

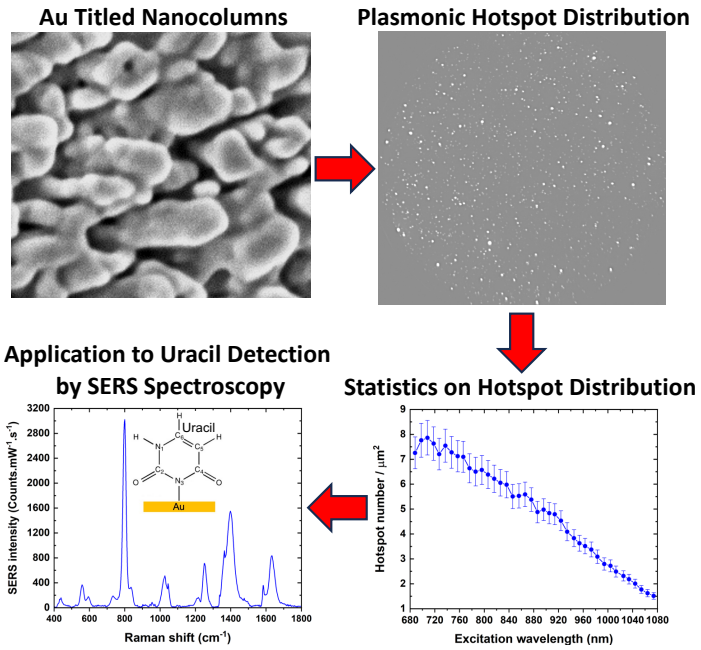

Highlights

Exploring plasmonic hotspots of Au tilted nanocolumns and their application to the uracil detection by surface-enhanced Raman scattering

Grégory Barbillon, Mathilde Faure, Ludovic Douillard, Eric Caudron, Christophe Humbert, José Miguel García-Martín

- Statistics on distribution of plasmonic hotspots (density and intensity) in the spectral range from 680 nm to 1080 nm.

- Correlation between SERS intensity and density/intensity of plasmonic hotspots.

- Sensitive detection of the uracil molecule at the concentration level of 6 nM.

Exploring plasmonic hotspots of Au tilted nanocolumns and their application to the uracil detection by surface-enhanced Raman scattering

Grégory Barbillon[a,b], Mathilde Faure[c], Ludovic Douillard[c], Eric Caudron[d], Christophe Humbert[e], José Miguel García-Martín[f]

[a]*EPF-Engineering School, 55 Avenue du Président Wilson, F-94230 Cachan, France.*
[b]*Sorbonne Université, CNRS, Laboratoire Interfaces et Systèmes Electrochimiques, LISE, F-75005 Paris, France.*
[c]*Université Paris-Saclay, CEA, CNRS, SPEC, F-91190 Gif-sur-Yvette, France.*
[d]*Université Paris-Saclay, Lipides, Systèmes Analytiques et Biologiques, F-91400 Orsay, France.*
[e]*Institut de Chimie Physique, Université Paris-Saclay, CNRS, UMR8000, F-91405 Orsay, France.*
[f]*Instituto de Micro y Nanotecnología (IMN-CNM), CSIC (CEI UAM+CSIC), Isaac Newton 8, 28760 Tres Cantos, Madrid, Spain.*

Abstract

In this work, an investigation on plasmonic hotspots of Au tilted nanocolumns and their application to the uracil detection by surface-enhanced Raman scattering (SERS) is addressed. These Au tilted nanocolumns are fabricated by employing a low-cost and easy-to-implement fabrication technique, which is the glancing angle deposition with magnetron sputtering. Moreover, these Au nanocolumns can generate a great density of highly confined electric field zones, called hotspots, located in the nanogaps between the nearest nanocolumns. The photoemission electron microscopy is employed to obtain the statistics on the distribution of these plasmonic hotspots with a high accuracy (spatial resolution of 10-20 nm) in the spectral range from 680 nm to 1080 nm. Thus, the SERS intensity can be correlated with the density and the intensity distribution of these plasmonic hotspots. Finally, the plasmonic hotspots of the Au nanocolumns are used to assess the limit of detection (LOD) of the uracil molecule by SERS. This LOD is determined at 6 nM demonstrating the good sensitivity of our Au nanocolumns compared to the existing literature.

Keywords: Surface-enhanced Raman scattering, Plasmonics, Photoemission electron microscopy, Glancing angle deposition, Hotspots, Uracil

1. Introduction

Over the last twenty years, the interest for the development of sensitive plasmonic substrates for the surface-enhanced Raman scattering (SERS) nanosensing has greatly grown owing to their localized surface plasmon resonance (LSPR) adaptable in the spectral range from visible to near-infrared domains [1, 2, 3, 4]. These localized plasmons can produce high confined electric fields (hotspots), thus inducing an improvement of the Raman signal when their LSPR are very close to the excitation wavelength employed for Raman experiments. Moreover, the plasmonic hotspots (HS) can be set by adjusting the nature, shape, and size of metallic nanostructures [5, 6, 7, 8, 9, 10]. To obtain these plasmonic nanosystems, several fabrication techniques are available as self-assembly methods [11, 12, 13, 14], lithographic technologies [15, 16, 17, 18, 19, 20, 21] some of which are used in the microelectronic industry for instance, and the methods of physical vapor deposition (PVD) [22, 23, 24, 25, 26]. Alternative SERS substrates emerged as the flexible SERS substrates produced with different techniques of fabrication [27, 28, 29]. For example, Zhou's group demonstrated the fabrication of flexible SERS substrates obtained by dispersing a solution of Au nanoparticles and expanded graphite on filter papers [30]. In another work, Lin's group produced this type of SERS substrates consisting of a PDMS film covered by Au nanosphere-coated polystyrene microspheres obtained by the method of layer-by-layer transfer [31]. Nevertheless, lithographic processes require long time and a high cost. Furthermore, different complex steps of chemical processes can be involved in the technology of self-assembly. Concerning PVD techniques, a smart technology is the oblique angle deposition (OAD) allowing the realization of alloy or only metal nanostructures serving as SERS substrates [32], for instance. Among PVD methods, the most suitable technique for industry is the magnetron sputtering, which is a low-cost and easy-to-implement fabrication technique, thus permitting a large-scale production on huge surfaces. For instance, Wang's group used the magnetron sputtering associated to a technique of surface-wrinkling for the production of 3D flexible SERS substrates composed of a film of wrinkled polydimethylsiloxane (PDMS) covered by silver nanoparticles [33]. Several metallic nanostructures can be realized with the OAD technique [34, 35, 36, 37] as nanocolumnar films, which are realized when the tilt angle (angle between the normal to the substrate and the atoms flux) is above 70° that is commonly called glancing angle deposition (GLAD). The obtained nanocolumns are very interesting for the SERS nanosensing, because they present confinements and enhancements of the electric field located in the nanogaps between the nearest nanocolumns (gap plasmons) [38, 39]. A great number of groups also demon-

Email address: gregory.barbillon@epf.fr (Grégory Barbillon)

strated the fabrication of SERS substrates by employing the GLAD or OAD techniques. The geometries obtained with these techniques are numerous, for instance, tilted Ag and Ag@Au nanorods, Au multimers, and nanoparticles composed of metal–insulator–metal, reaching enhancement factors (EFs) of around 10^5 – 10^8 for the Raman signal [40, 41, 42, 43, 44, 45, 46, 47].

Nonetheless, all these research groups did not necessarily consider the correlation between the SERS intensity and the intensity distribution/density of the plasmonic hotspots. In order to have a complete description of the phenomenon, the near-field distribution of the plasmonic nanosystems must be obtained. In general, the studies of the near-field distributions of these plasmonic nanosystems are obtained by using numerical simulations [48, 49, 50]. From an experimental point of view, the near-field can be observed by means of several techniques [51] such as scanning near-field optical microscopy (SNOM) [52, 53, 54, 55, 56], near-field ablation technique of a substrate (NFA) [57, 58], nonlinear fluorescence microscopy (NFM) [59, 60] and nonlinear photopolymerization (NPh) [61, 62]. Nevertheless, these techniques present limitations such as a possible perturbation of the evanescent field due to excitation of localized surface plasmon and lightning-rod geometric effects at the tip-surface junction (intrusive technique) and a low reproducibility of the tip for SNOM technique, permanent damages on samples for NFA technique, and a specific coating of the plasmonic nanosystems with a layer of photopolymers (or dyes) for NFM and NPh techniques, which alters the LSPR properties. Thereby, experimentally obtaining near-field images of plasmonic nanosystems with a very good spatial resolution stays a challenge. A non-intrusive experimental technique exists to obtain near-field pictures with a spatial resolution of 10–20 nm, it is the photoemission electron microscopy (PEEM) [63, 64, 65, 66]. The principle of the PEEM technique is related to the collection of electrons emitted from near-field hotspots. For Au nanostructures, the PEEM signal corresponds to collected electrons after a three-photon absorption process [67, 68], thus allowing to produce images in intensity with an excellent contrast. These PEEM images permit to distinguish the hotspot distribution on the surface of our SERS substrates. Therewith, numerous research groups have employed PEEM microscopy to investigate the near-field distribution and dynamics of plasmons on particles and substrates at the nanoscale [69, 70, 71, 72, 73, 74].

Herein, we present an investigation on the plasmonic hotspots of Au tilted nanocolumns realized by glancing angle deposition (magnetron sputtering). In previous works [38, 39], we have shown that such tilted nanocolumns exhibit good performance as SERS substrates due to the existence of hotspots, which had been experimentally determined in a small area measuring 500×500 nm^2 and at an excitation wavelength of 633 nm using near-field scanning optical microscopy. In this work, by using the photoemission electron microscopy, statistics on the intensity distribution and density of plasmonic hotspots are obtained on a wide spectral range from 680 nm to 1080 nm. Next, these plasmonic hotspots are used to detect the uracil molecule in order to assess the detection sensitivity of our Au nanocolumns. We choose here the uracil molecule because this biomolecule is involved in various biological processes ranging from the RNA formation to metabolic pathways in certain bacteria [75, 76], and through the generation of a certain number of DNA mutations [77]. Even so, its detection is relatively little studied in the literature [78, 79, 80, 81, 82]. Indeed, a large part of studies concerns the orientation taken by the uracil molecule during its adsorption on a metallic surface [83, 84, 85, 86].

2. Experimental Methods

2.1. Fabrication of the Au tilted nanocolumns

The nanocolumn film was prepared with magnetron sputtering in an UHV chamber (base pressure in the 10^{-10} mbar range) on a Si (110) substrate from Si-Mat (Kaufering, Germany) following the same process than in reference [39]. The magnetron source was supplied by AJA (North Scituate, MA, USA), a circular Au target of 3.8 cm in diameter was used, and the distance between substrate and target was 19 cm. An Ar plasma with 1.5 $\times$ 10^{-3} mbar base pressure was used for the sputtering. First, in the standard configuration with substrate parallel to the target, an initial bonding layer of Ti was deposited to improve the adhesion between the substrate and the subsequent Au layer. Direct current (DC) excitation at 100 W constant power was applied during 192 seconds to obtain a 5 nm thick Ti continuous film. Then, the substrate was tilted 84° to sputter Au in glancing angle deposition (GLAD) configuration and promote nanocolumn growth due to atomic shadowing mainly [87]. For Au, the DC power was 100 W and the deposition time was 20 minutes. After fabrication, the samples were kept in fluoroware wafer boxes in ambient conditions.

2.2. SEM Characterization

Scanning electron microscopy (SEM) with a FEI Verios 460 field emission microscope (FEI Europe B.V., Eindhoven, Netherlands) was used to determine the morphology and thickness of the Au nanocolumn film. The images were obtained with 2 kV acceleration voltage (i.e., low voltage) and 25 pA electron beam current in order to get a detailed definition of the surface. In the case of cross-section imaging, the sample was cut by cleavage.

2.3. Photoemission electron microscopy

Surface illumination is achieved using a pulsed mode-locked Ti:Al_2O_3 laser system (Chameleon Ultra II laser source, Coherent Inc.) delivering tunable photons in the wavelength range (680, 1080 nm), i.e., the energy range (1.15, 1.82 eV). The pulse repetition rate is fixed at 80 MHz. Each pulse exhibits a profile of 155 femtosecond (fs) duration. The excitation light beam is focused at grazing incidence (16° off surface plane) on the sample surface using a 150.5 mm focal length lens (Thorlabs LA4904). The polarization is transverse magnetic (i.e., *p*-polarized). The laser irradiance is in the range 0.15-0.3 GW/cm^2. Near-field images are acquired using a photoemission electron microscope (spectrometric LEEM/PEEM III, Elmitec GmbH) operating in ultrahigh vacuum at a pressure in the low range of 10^{-10} mbar. The PEEM fields of view range

from 1 to 120 µm, with a final spatial resolution better than 20 nm. The instrument operates in total electron yield (no energy filtering).

2.4. Processing of PEEM images

In PEEM imaging mode, the brightness measured in a given image area is proportional to the electron emission from that area. The collected electron emission reflects the optical near-field at the substrate surface. For a nanostructured surface made of Au, the photoemission signal scales as the sixth power of the local field $\propto (E_{local})^6$ [67]. Near-field hotspots are counted by image processing. Specifically, PEEM near-field images are cross-correlated with a representative hotspot signature (pattern recognition). Thresholding is then applied to the correlation product to extract the positions of the hotspots within the image. Knowing the positions of hotspots in an image provides access to various near-field characteristics such as hotspot surface density, averaged intensity, and intensity histograms, for instance. Image processing is performed using a homemade software (ImaGo developed by L. Douillard CEA IRAMIS SPEC, see Appendix for more details in the processing of PEEM images).

2.5. Uracil Deposition

To do the aqueous solutions of uracil (>99%, ThermoFisher) at neutral pH, the uracil powder is diluted to a concentration of 10^{-3} M by using deionized water (18.2 MΩ), then sonicated during around 30 min up to the complete dissolution of the powder. Next, this solution is diluted with deionized water at concentrations ranging from 10^{-4} M to 10^{-9} M. 60 µL of each uracil solution are deposited on Au nanocolumns, next dried at room temperature.

2.6. Reflectance and Raman Spectroscopies

Differential reflectance spectroscopy is performed using a Cary-5000 spectrophotometer (Agilent) in reflection configuration of unpolarized light reaching the sample with an incidence angle of 7° with respect to the normal direction to the sample surface. The reference spectrum is bare silicon prior nanocolumn deposition. The reflectance is obtained from the following definition: Reflectance = $\log_{10}(R_0/R)$ where R_0 and R are the reflectivity measurements of the silicon substrate without and with Au nanocolumns, respectively [88, 89]. SERS spectra are acquired using a commercial spectrometer from Horiba Scientific. The employed model is a Labram HR with an excellent spectral resolution (< 3 cm^{-1}). The chosen wavelength of excitation is 785 nm with a laser power of 2.2 mW, a wavelength in the spectral range (680–1080 nm) of our PEEM study. The acquisition time is adjusted at 2 s. The focus of the excitation laser on Au nanocolumns is realized through a microscope objective (N.A. = 0.75; ×80). By this objective, we also collect SERS signals coming from our samples. The mean of SERS intensities and relative standard deviations (RSD) are determined with the acquisition of 10 SERS spectra at different positions taken randomly on Au nanocolumns. All SERS experiments have been obtained at least two weeks after the substrate fabrication, some of them were even used after several months, and no difference was observed.

3. RESULTS AND DISCUSSION

In the first place, the Au nanocolumns are fabricated by using the process described in section 2.1, then characterized by SEM. The figure 1a,b shows representative SEM images of the Au nanocolumns, from the top and in cross-section. Nanocolumns can be observed tilted towards the direction of atomic flow during deposition (yellow arrow in the figure 1a,b), and the tilt angle of the nanocolumns with respect to the substrate normal is $\beta = 60°$, in excellent agreement with previous results for Au [90]. From cross-section images, the thickness of the nanocolumnar film is about 75 nm and the average diameter of the nanocolumns is 26 ± 4 nm. However, as it can be seen in the top view images, some nanocolumns coalesce in the direction transverse to their axis, since the atomic shadowing mechanism that induces the development of the nanocolumn morphology in the GLAD configuration only acts in the direction of the incoming atomic flux, and thus does not limit the growth in that transverse direction. In addition, the reflectance spectrum of Au tilted nanocolumns is performed and displayed in the figure 1c.

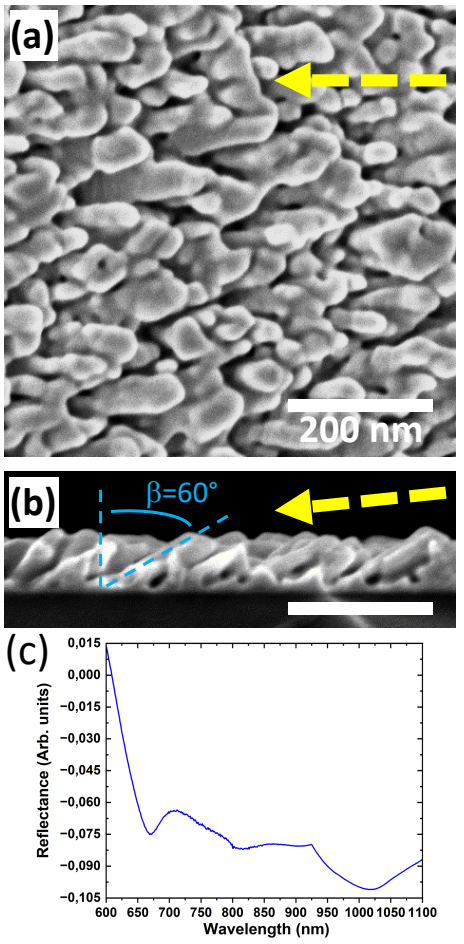

Figure 1: Representative SEM pictures of Au nanocolumnar thin films: (a) top-view and (b) cross-section. The white scale bar is 200 nm in both pictures. The yellow dotted arrow indicates the projection of the atomic flux direction during the Au deposition, and β is the tilt angle of the nanocolumns. (c) Reflectance spectrum of Au tilted nanocolumns.

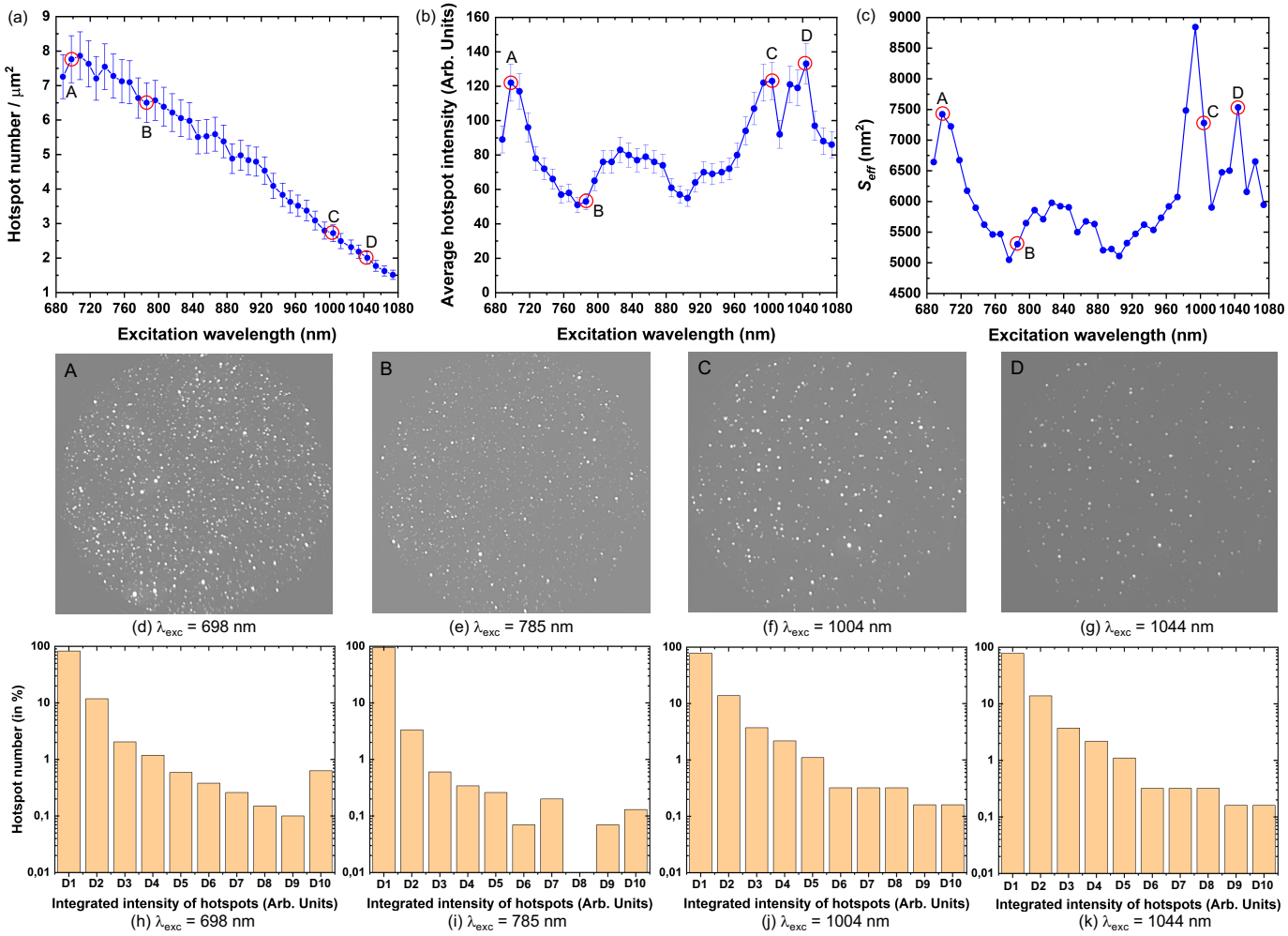

Figure 2: (a) HS surface density, (b) average HS intensity, and (c) mean effective surface of one hotspot (S_{eff}) versus excitation wavelength on the spectral range of 680–1080 nm. PEEM images of Au nanocolumnar thin film (field of view = 16.7 µm in diameter) recorded at different excitation wavelengths (λ_{exc}): (d) 698 nm (Pt A), (e) 785 nm (Pt B), (f) 1004 nm (Pt C) and (g) 1044 nm (Pt D), and their respective histograms of the integrated intensity distribution of hotspots: (h) 698 nm, (i) 785 nm, (j) 1004 nm and (k) 1044 nm, where D1 to D10 represent the deciles from the first to the tenth for the integrated intensity of hotspots.

From this latter, several more or less pronounced "dips" can be distinguished corresponding to plasmonic resonances [81, 89, 91] due to the coupling of the localized surface plasmon resonance (LSPR) of the individual nanocolumns, thus broadening and redshifting the LSPR band. Next, the Au nanocolumns are characterized by PEEM to obtain hotspot images as well as their distribution statistics on the surface of Au nanocolumns in the spectral range of 680–1080 nm. Figure 2a,b,c represents the hotspot surface density as a function of excitation wavelength as well as the average intensity of the hotspots and the mean effective surface of one hotspot (S_{eff}). Figure 2a shows that the surface density of hotspots decreases linearly with the excitation wavelength. This behaviour is consistent with the scaling law predicted in the infrared domain for $\omega_p \gg \omega$ [67, 92, 93], where ω_p is the Au plasma frequency (ω_p = 8.45 eV (146 nm) for a thin film of Au [94]). In the figure 2b, we note high values of average HS intensity located around 700 nm and in the IR region (980–1080 nm). Next, we observe high values of S_{eff} located in these same regions, as displayed in the figure 2c.

In addition, the figure 2,d,e,f,g displays four representative images of hotspots distributed on the surface of the Au nanocolumnar film. Three of these images are recorded at maximum values of the average HS intensity (named A, C, and D, see figure 2b), and the remaining one (named B in figure 2b) is recorded at the excitation wavelength (785 nm) that is used for the SERS experiments. Moreover, these maximum values of the average HS intensity are rather in good agreement with the plasmonic resonances ("dips") observed in the reflectance spectrum (see figure 1c), and for the value of the average HS intensity recorded at 785 nm, this latter is close to a plasmonic resonance around 812 nm (see this less pronounced "dip" in figure 1c). Furthermore, the respective histograms of the hotspot intensity distribution associated to these four images are displayed in figure 2h,i,j,k. Examination of the histograms shows a large number of low-intensity hotspots. Whatever the excitation wavelength, the number of hotspots in the first decile represents a fraction in excess of 75%, this fraction becomes 97.5%

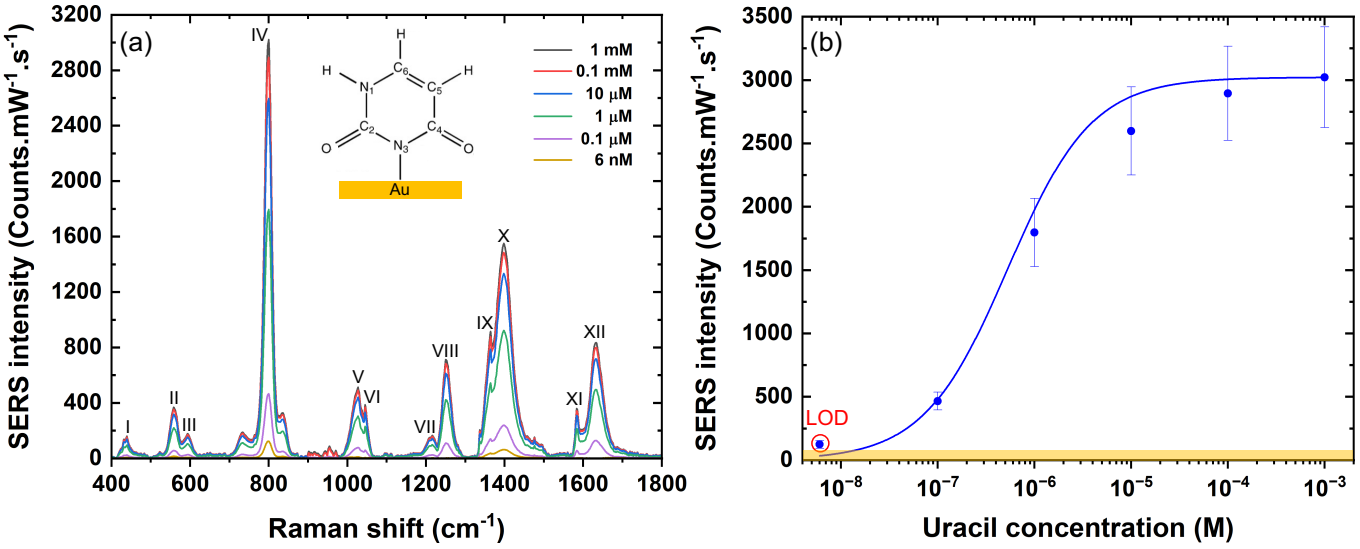

Figure 3: (a) SERS spectra recorded at the excitation wavelength of 785 nm for uracil concentration ranging from 1 mM to 6 nM. The numbers from I to XII correspond to the characteristic Raman peaks of the uracil molecule. The inset depicts the orientation scheme of the uracil molecule on Au nanocolumns. (b) SERS intensity as a function of the uracil concentration (M), and the blue dots and the blue line correspond to experimental data and the fit with the Langmuir-type model (R^2 = 0.981), respectively. The red circle corresponds to the detection limit (LOD), and the orange rectangle represents the zone of noise level.

below the median class. Statistically, the relative fraction of intense hotspots increases with wavelength. For example, if we consider the population of hotspots above the first decile (D1), i.e., the 9/10 of the hotspot population above the 1/10 least intense hotspots, its evolution increases with wavelength: hotspot population fraction (> D1, in %) is 17% at 698 nm, 5% at 785 nm, 22% at 1004 nm, and 25% at 1044 nm. Overall, combined with the linear decrease of the hotspot surface density with the excitation wavelength, the average number of intense hotspots (> D1) presents a minimum in the middle part of the probed wavelength interval, as suggested by the average value of hotspot intensity (see figure 2b). The average number of intense hotspots (> D1) within a circular field of view of radius 8.3 µm (218 µm^2) is 320 HS at 698 nm, 76 HS at 785 nm, 143 HS at 1004 nm, and 110 HS at 1044 nm. In summary, the points A, C, and D would be very interesting to use for SERS experiments, but we have a unique excitation wavelength (here 785 nm corresponding to the point B) included in the spectral range (680–1080 nm) of our PEEM study. Nevertheless, the point B remains interesting because the number of hotspots is important even with a lower average HS intensity. Moreover, we demonstrated by using finite-difference time-domain simulation in a previous work [38] that the enhancement factor of the electric field $|E|/|E_0|$ reached a value of up to 30 at the excitation wavelength of 785 nm due to the LSPR coupling of the individual nanocolumns, broadening and redshifting the LSPR band, confirmed here by the reflectance spectrum of the Au tilted nanocolumns. This high HS number allows for reaching a good sensitivity of detection, and therefore, we apply it for determining this latter regarding the uracil molecule, by SERS.

To assess the detection sensitivity of our Au tilted nanocolumns, we functionalize them with uracil by employing the method described in section 2.5. Next, SERS spectra are acquired at the excitation wavelength of 785 nm. On the SERS spectrum recorded at the 1 mM concentration shown in Figure 3a, twelve Raman peaks characteristic of the uracil molecule are well discerned [83, 84, 95](see Table 1). The appearance of these Raman peaks indicates that the adsorption structure of the uracil molecule is in its form tautomer II (i.e., the bond Au–N is on the atom N3, see the inset of the figure 3a) and perpendicular to the surface of Au nanocolumns [83, 84].

In order to establish the limit of detection threshold for uracil molecules, we opt for the most intense Raman peak located at 800 cm^{-1}. SERS spectra are acquired for uracil concentrations ranging from 6 nM to 1 mM (see Figure 3a). Next, we plot the SERS intensity of the chosen peak as a function of the uracil concentration (see Figure 3b). The uniformity of the SERS signal on Au nanocolumns is assessed by recording its intensity

Table 1: Characteristic Raman peaks of the uracil molecule (δ = in-plane bending, ν = stretching, see also the inset of the figure 3a for C2, C4, C5, C6, and N1).

Ref.	Raman shift (cm^{-1})	Vibration modes
I	439	δ(C2=O, C4=O)
II	558	Ring deformation
III	593	Ring deformation
IV	800	Ring breathing
V	1027	ν(ring), δ(C6–H)
VI	1045	Ring deformation
VII	1216	ν(C6–N), δ(N1–H, C5–H, C6–H)
VIII	1251	ν(C4–N), δ(N1–H, C5–H, C6–H)
IX	1364	ν(C4=O), δ(N1–H, C6–H)
X	1395	δ(N1–H, C5–H, C6–H)
XI	1584	ν(C4=O), δ(N1–H, C6–H)
XII	1630	ν(C2=O) + ν(C4=O), δ(N1–H)

at 800 cm^{-1} on 10 different locations of the sample taken randomly. The relative standard deviation (RSD) is determined (see error bars in Figure 3b) with a mean value of RSD inferior or equal to 15% for all experimental values. A limit of the detection threshold (LOD) of 6 nM is achieved for Au tilted nanocolumns, defined as a SERS signal significantly above the noise level. More precisely, the latter is determined with the following definition in [96]: minimum intensity level = I_{blank} + $k\sigma_{blank}$, where I_{blank} is the average value of the SERS intensity of blank (i.e., without uracil) at Raman peak of 800 cm^{-1} (in our case), σ_{blank} is the associated standard deviation and k is a factor chosen with a confidence level of 95% (here $k = 3$). From the SERS spectra displayed in Figure 3a, we determine that the minimum intensity level is 104 Counts.$mW^{-1}.s^{-1}$ (I_{blank} = 68 Counts.$mW^{-1}.s^{-1}$, σ_{blank} = 12 Counts.$mW^{-1}.s^{-1}$). This minimum intensity level is represented by the orange rectangle in Figure 3b. Note also that the determined LOD doesn't take into account potential interference from molecules structurally similar to the target uracil molecule like urea and/or uric acid or even other nucleobases (e.g., adenine, guanine). We assume that this LOD is due to the important number of hotspots present on Au nanocolumns sample at this excitation wavelength of 785 nm rather than to their average intensity. Furthermore, this LOD is better than those obtained with polymethylmethacrylate optical fibers covered by a layer of polyvinylidene fluoride and Ag nanoparticles (LOD = 384 nM, [78]), plasmonic hierarchical nanoaggregates in form of raspberry (LOD = 300 nM, [79]), hybrid plasmonic nanojunctions (LOD = 27 nM, [80]), plasmonic aluminum nanohole arrays (LOD = 1 nm of uracil molecule thickness, [81]), and of the same magnitude order than that of aligned diphenylalanine nanotubes coated with Ag nanoparticles (LOD $\approx$ 1 nM, [82]). Next, figure 3b shows a fit of the SERS experimental data using a Langmuir-type model, as follows [97, 98, 99]:

$$I = I_{max}\frac{K_{ad}C_{ura}}{1+K_{ad}C_{ura}} \quad (1)$$

where C_{ura} represents the investigated concentration of uracil, and K_{ad} is the adsorption constant. I describes the SERS intensity at the concentration C_{ura}. I_{max} corresponds to the highest value of the SERS intensity corresponding to the complete formation of an uracil monolayer. Therewith, we report a good agreement between the experimental values and the Langmuir model depicted in Figure 3b (see the blue line). K_{ad} is determined from this model and K_{ad} is 1.9 $\times$ 10^6 M^{-1}. This value highlights a good affinity of adsorption for the uracil molecule on the Au nanocolumns. By analogy, the Langmuir-type model also allows to determine the coverage rate of the uracil molecule σ_{mol} as a function of its concentration in the aqueous solution using the equation 2 [100], where $\sigma_{max} = 7.79 \times 10^{-10}$ mol/cm^2 represents the surface coverage of an uracil monolayer (vertical position) on an Au surface [101]. At the limit of detection, we obtain a coverage rate σ_{mol} / σ_{max} = 0.0113.

$$\sigma_{mol} = \sigma_{max}\frac{K_{ad}C_{ura}}{1+K_{ad}C_{ura}} \quad (2)$$

As an illustration, this coverage rate can be easily translated into the number of molecules probed in the Raman experiment, based on knowledge of the active SERS surface area. As a first approximation, the active SERS surface (S_{HS}) inside the laser focus corresponds to the cumulative sum of the effective areas of the numerous individual hotspots: $S_{HS} = S_{Focus} \times D_{HS} \times S_{eff}$, where S_{Focus} is the laser spot area (S_{Focus} = 1.28 μm^2 [102]), D_{HS} is the surface density of the hotspots at the working wavelength whatever the hotspot intensity. D_{HS} is extracted from figure 2a, D_{HS} = 6.5 hotspots/μm^2 (at 785 nm). S_{eff} corresponds to the average effective area of one single hotspot. This effective area can be estimated from the PEEM near-field maps and corresponds to an average value of 5.304 $\times$ 10^{-3} μm^2 at λ_{exc} = 785 nm (see figure 2c). Note that this (over)estimate is an approximate value, uncorrected for the point spread function (PSF) of the electron optics of the photoemission microscope, and also that the mean effective area determined by PEEM is assumed to be valid for SERS measurements ($S_{eff(PEEM)}$ = $S_{eff(SERS)}$). This point is valid only as a first approximation, since the illumination regimes are distinct between the two experiments. This gives an active surface S_{HS} = 4.41 $\times$ 10^{-2} μm^2 within the laser focus. The number of probed molecules N_{mol} is the product of the molecular coverage rate σ_{mol} extracted at the detection limit (Langmuir-type model) by the calculated active SERS surface S_{HS}: $N_{mol} = N_{Avo} \times \sigma_{mol} \times S_{HS}$, where N_{Avo} is the Avogadro number. We obtain a total number of probed molecules of 2334 at the limit of detection, i.e., an average of 281 probed molecules per hotspot, whatever its intensity at 785 nm excitation wavelength. Figure 4 illustrates the SERS signal intensity vs number of probed molecules for both population sets.

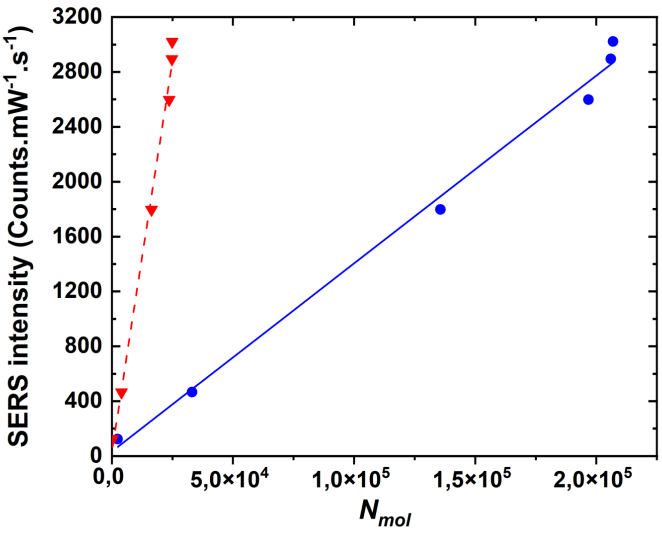

Figure 4: SERS intensity as a function of N_{mol}, where red triangles and blue dots represent the experimental results for the number of uracil molecules detected per hotspot and on hotspots present in the laser spot area, respectively. The dashed red and solid blue curves are the linear fits of which equations are $y = 0.114x + 34.13$ (R^2 = 0.993) and $y = 0.0137x + 34.15$ (R^2 = 0.993), respectively.

4. CONCLUSION

In this investigation, we obtained distribution statistics of hotspots for Au tilted nanocolumns by using the photoemission electron microscopy in the spectral range from 680 nm to 1080 nm by step of 10 nm with a spatial resolution down to 20 nm. PEEM data confirmed the linear decay law of the hotspot surface density as a function of wavelength in the near infrared wavelength range. Next, a sensitive SERS detection of uracil molecules was realized by employing these Au tilted nanocolumns fabricated with magnetron sputtering in glancing angle deposition configuration (low-cost technique). A limit of detection threshold of 6 nM was achieved for Au tilted nanocolumns close to those reached with the different SERS substrates published in literature. We reported that this detection limit was due to the important number of hotspots present on Au nanocolumns sample rather than to their average intensity, recorded at the excitation wavelength of this investigation. Furthermore, a uniform SERS signal for Au tilted nanocolumns with an average RSD $\leqslant 15\%$ was evidenced as well as a value of the adsorption coefficient K_{ad} of 1.9×10^6 M^{-1} for uracil molecules on our Au tilted nanocolumns, indicating a good affinity of adsorption between them. Henceforth, this investigation can offer the possibility of a commercial/industrial production of these SERS substrates with an easy-to-implement and low-cost technique of manufacturing on wide surfaces after supplementary studies on their selectivity, batch-to-batch reproducibility, and stability.

CRediT authorship contribution statement

G. Barbillon: Conceptualization, Formal analysis, Investigation, Resources, Supervision, Validation, Visualization, Writing – original draft, Writing – review & editing. **M. Faure:** Investigation, Resources, Writing – review & editing. **L. Douillard:** Formal analysis, Investigation, Resources, Supervision, Validation, Visualization, Writing – original draft, Writing – review & editing. **E. Caudron:** Investigation, Resources, Writing – review & editing. **J.M. García-Martín:** Formal analysis, Investigation, Resources, Supervision, Validation, Visualization, Writing – original draft, Writing – review & editing.

Declaration of competing interest

The authors declare that they have no known competing financial interests or personal relationships that could have appeared to influence the work reported in this paper.

Acknowledgements

José Miguel García-Martín thanks grant PID2021-126524NB-I00 funded by MCIN/AEI/10.13039/501100011033 and by "ERDF A way of making Europe", and also acknowledges the service from the MiNa Laboratory at IMN, funded from CM (project SpaceTec, S2018/NMT-4291 TEC2SPACE), MINECO (project CSIC13-4E-1794), and EU (FEDER, FSE).

Appendix. Details on PEEM image processing

The starting point of the statistical analysis is an image of hotspots obtained by photoemission electron microscopy at a given wavelength and irradiance of the laser light source (see figure 2,d,e,f,g). Each image contains several hundred hotspots of various intensities Int_i. The aim of image processing is to extract from such an image a list of hotspots in the form of a list of triplets $(x_i, y_i, \mathrm{Int}_i)$, where (x_i, y_i) correspond to the hotspot coordinates (in pixels) of the point of index i in the large image and Int_i represents its PEEM intensity in arbitrary units. This list is the entry point for more advanced statistical processing aimed at obtaining important statistical quantities of the point distribution, such as the average distance between points, the histograms of intensities, and the surface density, for instance.

The $(x_i, y_i, \mathrm{Int}_i)$ list of hotspots is obtained in two steps: the first step is to obtain a binary image (two-level coding depth = (black, white) = (0, 1)) of the hotspot positions, the second step is to multiply this two-level image with the original source image and extract the maxima in the form of a list $(x_i, y_i, \mathrm{Int}_i)$.

Extraction of the hotspot positions is based on the detection of a generic hotspot feature via a normalized cross-correlation (NCC) routine. The home-made image processing software ImaGo implements the normalized cross-correlation as described in [103]. The first step is to select a generic hotspot, a template window of size $(2n+1) \times (2n+1)$ pixels^2. The objective of the recognition procedure is to find instances of the reference template in a large image by shifting the template window in a pixel-by-pixel basis and computing the normalized correlation between them at each (x, y) position. The normalized cross-correlation function is bounded on the interval $[-1, 1]$, a value close to unity indicating a good match between the reference template window and the processed image feature. The normalized cross-correlation image is then thresholded to retain only the most intense hotspots close in shape to the reference mask (i.e., the background noise is eliminated). Hotspot positions are obtained by extracting the maxima of the thresholded distribution of the normalized cross-correlation values. Note that the same reference template window (generic hotspot) is kept for wavelength image series analysis.

In the home-made image processing software ImaGo, the NCC is conducted with a template window 9×9 pixels^2 in size ($n = 4$, user selection). This size is chosen so as to detect close pairs of hotspots (without overlap). The NCC threshold is fixed so as to retain a normalized cross-correlation value $\geqslant 0.9$. The other classic image processing routines (kernel filtering, simple operations on image), in particular the maxima extraction routine, are implemented in accordance with the procedures presented in [104].

Data availability

Data will be made available on request.

References

[1] K. A. Willets, R. P. Van Duyne, Localized Surface Plasmon Resonance Spectroscopy and Sensing, Annu. Rev. Phys. Chem. 58 (2007) 267–297.

[2] S. Barbosa, A. Agrawal, L. Rodríguez-Lorenzo, I. Pastoriza-Santos, R. A. Alvarez-Puebla, A. Kornowski, H. Weller, L. M. Liz-Marzan, Tuning Size and Sensing Properties in Colloidal Gold Nanostars, Langmuir 26 (2010) 14943–14950.

[3] G. A. Vinnacombe-Willson, Y. Conti, A. Stefancu, P. S. Weiss, E. Cortés, L. Scarabelli, Direct Bottom-Up *In Situ* Growth: A Paradigm Shift for Studies in Wet-Chemical Synthesis of Gold Nanoparticles, Chem. Rev. 123 (2023) 8488–8529.

[4] G. Barbillon, H. Cheap-Charpentier, Advances in Surface-Enhanced Raman Scattering Sensors of Pollutants in Water Treatment, Nanomaterials 13 (2023) 2417.

[5] S. Lal, N. K. Grady, J. Kundu, C. S. Levin, J. B. Lassiter, N. J. Halas, Tailoring plasmonic substrates for surface enhanced spectroscopies, Chem. Soc. Rev. 37 (2008) 898–911.

[6] M. J. Banholzer, J. E. Millstone, L. Qin, C. A. Mirkin, Rationally designed nanostructures for surface-enhanced Raman spectroscopy, Chem. Soc. Rev. 37 (2008) 885–897.

[7] M. D. Sonntag, J. M. Kilngsporn, A. B. Zrimsek, B. Sharma, L. K. Ruvuna, R. P. Van Duyne, Molecular plasmonics for nanoscale spectroscopy, Chem. Soc. Rev. 43 (2014) 1230–1247.

[8] S. -Y. Ding, E. -M. You, Z. -Q. Tian, M. Moskovits, Electromagnetic theories of surface-enhanced Raman spectroscopy, Chem. Soc. Rev. 46 (2017) 4042–4076.

[9] G. Barbillon, A. Ivanov, A. K. Sarychev, Hybrid Au/Si Disk-Shaped Nanoresonators on Gold Film for Amplified SERS Chemical Sensing, Nanomaterials 9 (2019) 1588.

[10] G. Barbillon, Nanoplasmonics in High Pressure Environment, Photonics 7 (2020) 53.

[11] P. Wu, L. -B. Zhong, Q. Liu, X. Zhou, Y. -M. Zheng, Polymer induced one-step interfacial self-assembly method for the fabrication of flexible, robust and free-standing SERS substrates for rapid on-site detection of pesticide residues, Nanoscale 11 (2019) 12829–12836.

[12] Z. Fusco, R. Bo, Y. Wang, N. Motta, H. Chen, A. Tricoli, Self-assembly of Au nano-islands with tuneable organized disorder for highly sensitive SERS, J. Mater. Chem. C 7 (2019) 6308–6316.

[13] Z. Lao, Y. Zheng, Y. Dai, Y. Hu, J. Ni, S. Ji, Z. Cai, Z. J. Smith, J. Li, L. Zhang, D. Wu, J. Chu, Nanogap Plasmonic Structures Fabricated by Switchable Capirally-Force Driven Self-Assembly for Localized Sensing of Anticancer Medicines with Microfluidic SERS, Adv. Funct. Mater. 30 (2020) 1909467.

[14] Z. Yin, Y. Zhou, P. Cui, J. Liao, M. H. Rafailovich, W. Sun, Fabrication of ordered bi-metallic array with superstructure of gold micro-rings via templated-self-assembly procedure and its SERS applications, Chem. Commun. 56 (2020) 4808–4811.

[15] G. Barbillon, J. -L. Bijeon, G. Lérondel, J. Plain, P. Royer, Detection of chemical molecules with integrated plasmonic glass nanotips, Surf. Sci. 602 (2008) L119–L122.

[16] A. Dhawan, A. Duval, M. Nakkach, G. Barbillon, J. Moreau, M. Canva, T. Vo-Dinh, Deep UV nano-microstructuring of substrates for surface plasmon resonance imaging, Nanotechnology 22 (2011) 165301.

[17] N. G. Quilis, S. Hageneder, S. Fossati, S. K. Auer, P. Venugopalan, A. Bozdogan, C. Petri, A. Moreno-Cencerrado, J. L. Toca-Herrera, U. Jonas, J. Dostalek, UV-Laser Interference Lithography for Local Functionalization of Plasmonic Nanostructures with Responsive Hydrogel, J. Phys. Chem. C 124 (2020) 3297–3305.

[18] A. -C. Faure, G. Barbillon, M. Ou, G. Ledoux, O. Tillement, S. Roux, D. Fabregue, A. Descamps, J. -L. Bijeon, C. A. Marquette, C. Billotey, C. Jamois, T. Benyatou, P. Perriat, Core/shell nanoparticles for multiple biological detection with enhanced sensitivity and kinetics, Nanotechnology 19 (2008) 485103.

[19] V. R. Manfrinato, F. E. Camino, A. Stein, L. H. Zhang, M. Lu, E. A. Stach, C. T. Black, Patterning Si at the 1 nm Length Scale with Aberration-Corrected Electron-Beam Lithography: Tuning of Plasmonic Properties by Design, Adv. Funct. Mater. 29 (2019) 1903429.

[20] C. Farcau, D. Marconi, A. Colnita, I. Brezestean, L. Barbu-Tudoran, Gold Nanospot-Shell Arrays Fabricated by Nanoimprint Lithography as a Flexible Plasmonic Sensing Platform, Nanomaterials 9 (2019) 1519.

[21] Y. F. C. Chau, K. H. Chen, H. P. Chiang, C. M. Lim, H. J. Huang, C. H. Lai, N. T. R. N. Kumara, Fabrication and Characterization of a Metallic-Dielectric Nanorod Array by Nanosphere Lithography for Plasmonic Sensing Applications. Nanomaterials 9 (2019) 1691.

[22] J. -H. Han, D. Kim, J. Kim, G. Kim, P. Fischer, H. -H. Jeong, Plasmonic Nanostructure Engineering with Shadow Growth, Adv. Mater. 35 (2023) 2107917.

[23] B. Ai, Y. Zhao, Glancing angle deposition meets colloidal lithography: A new evolution in the design of nanostructures, Nanophotonics 8 (2019) 1–26.

[24] Y. Liu, J. Liu, S. Sohn, Y. Li, J. J. Cha, J. Schroers, Metallic glass nanostructures of tunable shape and composition, Nat. Commun. 6 (2015) 7043.

[25] Z. Huang, F. Bai, Wafer-scale, three-dimensional helical porous thin films deposited at a glancing angle, Nanoscale 6 (2014) 9401–9409.

[26] A. G. Mark, J. G. Gibbs, T. -C. Lee, P. Fischer, Hybrid nanocolloids with programmed three-dimensional shape and material composition. Nat. Mater. 12 (2013) 802–807.

[27] J. Zhang, J. Wu, B. Wang, Y. Geng, Z. Wang, A new strategy for constructing 3D hybrid graphene/Au/rectangular pyramids PMMA on a flexible SERS substrate for trace molecule detection, Sens. Actuators B Chem. 410 (2024) 135711.

[28] H. Liu, Y. He, K. Cao, Flexible Surface-Enhanced Raman Scattering Substrates: A Review on Constructions, Applications, and Challenges, Adv. Mater. Interfaces 8 (2021) 2100982.

[29] T. Jing, R. Gao, C. Zhan, Y. Yu, X. Chen, Y. Lu, H. K. Nam, Y. -J. Kim, L. Yu, Flexible surface-enhanced Raman scattering substrates: A review on design strategies, fabrication technologies, and applications, Coord. Chem. Rev. 539 (2025) 216739.

[30] S. Yi, M. Yang, Y. Yu, Z. Li, D. Zhang, F. Han, A. Grishko, Y. Li, Q. Qin, B. Zhou, Highly sensitive flexible SERS substrates with a sandwich structure for rapid detection of trace pesticides residues, Appl. Surf. Sci. 654 (2024) 159455.

[31] Y. Li, M. Dong, C. Li, M. Zhang, J. Zhang, S. Lin, Au Nanospheres Assembled on Polystyrene Microsphere Arrays on PDMS as Flexible SERS Substrates for Determination of Fungicides on Fish, ACS Appl. Nano Mater. 7 (2024) 25815–25822.

[32] P. Eiamchai, C. Chananonnawathorn, M. Horprathum, V. Patthanasettakul, S. Limwichean, N. Nuntawong, Spatial elemental investigations in nanostructured alloyed Ag/Au SERS substrates by magnetron sputtering oblique-angle co-deposition towards increased performance and shelf life, Appl. Surf. Sci. 513 (2020) 145748.

[33] H. Zhang, N. Zhao, H. Li, M. Wang, X. Hao, M. Sun, X. Li, Z. Wang, H. Yu, C. Tian, C. Wang, 3D Flexible SERS Substrates Integrated with a Portable Raman Analyzer and Wireless Communication for Point-of-Care Application, ACS Appl. Mater. Interfaces 14 (2022) 51253–51264.

[34] A. Barranco, A. Borras, A. R. Gonzalez-Elipe, A. Palmero, Perspectives on oblique angle deposition of thin films: From fundamentals to devices, Prog. Mater. Sci. 76 (2016) 59–153.

[35] Y. He, Y. Zhao, Advanced multi-component nanostructures designed by dynamic shadowing growth, Nanoscale 3 (2011) 2361–2375.

[36] L. Abelmann, C. Lodder, Oblique evaporation and surface diffusion, Thin Solid Films 305 (1997) 1–21.

[37] K. Robbie, M. J. Brett, A. Lakhtakia, Chiral sculptured thin films, Nature 384 (1996) 616.

[38] P. Díaz-Nuñez, J. M. García-Martín, M. U. González, R.González-Arrabal, A. Rivera, P. Alonso-González, J. Martín-Sánchez, J. Taboada-Gutiérrez, G. González-Rubio, A. Guerrero-Martínez, L. Bañares, O. Peña-Rodríguez, On the Large Near-Field Enhancement on Nanocolumnar Gold Substrates, Sci. Rep. 9 (2019) 13933.

[39] G. Barbillon, C. Humbert, M. U. González, J. M. García-Martín, Gold Nanocolumnar Templates for Effective Chemical Sensing by Surface-Enhanced Raman Scattering, Nanomaterials 12 (2022) 4157.

[40] Y. Yang, Z. Hu, Y. Wang, B. Wang, Q. Zhan, Y. Zhang, X. Ao, Broadband SERS substrates by oblique angle deposition method, Opt. Mater. Express 6 (2016) 2644–2654.

[41] H. O. Chu, S. Song, C. Li, D. Gibson, Surface Enhanced Raman Scattering Substrates Made by Oblique Angle Deposition: Methods and Applications, Coatings 7 (2017) 26.

[42] S. K. Gahlaut, D. Savargaonkar, C. Sharan, S. Yadav, P. Mishra, J. P. Singh, SERS Platform for Dengue Diagnosis from Clinical Samples Employing a Hand Held Raman Spectrometer, Anal. Chem. 92 (2020) 2527–2534.

[43] Y. Kang, X. Xue, W. Wang, Y. Fan, W. Li, T. Ma, F. Zhao, Z. Zhang, Design of Armrest Ag Nanorod Arrays with High SERS Performance for

Sensitive Biomolecule Detection, J. Phys. Chem. C 124 (2020) 21054–21062.
[44] P. Sha, Q. Su, P. Dong, T. Wang, C. Zhu, W. Gao, X. Wu, Fabrication of Ag@Au (core@shell) nanorods as a SERS substrate by the oblique angle deposition process and sputtering technology, RSC Adv. 11 (2021) 27107–27114.
[45] C. -M. Tsen, C. -W. Yu, S. -Y. Chen, C. -L. Lin, C. -Y. Chuang, Application of surface-enhanced Raman scattering in rapid detection of dithiocarbamate pesticide residues in foods, Appl. Surf. Sci. 558 (2021) 149740.
[46] S. Yadav, R. Khanam, J. P. Singh, A purview into highly sensitive magnetic SERS detection of hemozoin biomarker for rapid malaria diagnosis, Sens. Actuator B Chem. 355 (2022) 131303.
[47] Z. R. Lawson, A. S. Preston, M. T. Korsa, N. L. Dominique, W. J. Tuff, E. Sutter, J. P. Camden, J. Adam, R. A. Hughes, S. Neretina, Plasmonic Gold Trimers and Dimers with Air-Filled Nanogaps, ACS Appl. Mater. Interfaces 14 (2022) 28186–28198.
[48] W. Yue, Z. Wang, J. Whittaker, F. Lopez-royo, Y. Yang, A. V. Zayats, Amplification of surface-enhanced Raman scattering due to substrate-mediated localized surface plasmons in gold nanodimers, J. Mater. Chem. C 5 (2017) 4075–4084.
[49] Y. Huang, Y. Chen, L. -L. Wang, E. Ringe, Small morphology variations effects on plasmonic nanoparticle dimer hotspots, J. Mater. Chem. C 6 (2018) 9607–9614.
[50] Q. Zhu, C. Xu, D. Wang, B. Liu, F. Qin, Z. Zhu, Y. Liu, X. Zhao, Z. Li, Femtomolar response of a plasmon-coupled ZnO/graphene/silver hybrid whispering-gallery mode microcavity for SERS sensing, J. Mater. Chem. C 7 (2019) 2710–2716.
[51] R. Bachelot, L. Douillard, Probing the Optical Near–Field, in: R. Gordon (Eds.), Advances in Near–Field Optics, Springer Series in Optical Sciences, vol 244. Springer, Cham, 2023, pp. 137–196.
[52] M. Rang, A. C. Jones, F. Zhou, Z. Y. Li, B. J. Wiley, Y. Xia, M. B. Raschke, Optical near-field mapping of plasmonic nanoprisms, Nano Lett. 8 (2008) 3357–3363.
[53] K. Imura, K. Ueno, H. Misawa, H. Okamoto, Anomalous light transmission from plasmonic-capped nanoapertures, Nano Lett. 11 (2011) 960–965.
[54] Y. Tanaka, H. Ishiguro, H. Fujiwara, Y. Yokota, K. Ueno, H. Misawa, K. Sasaki, Direct imaging of nanogap-mode plasmon-resonant fields, Opt. Express 19 (2011) 7726–7733.
[55] A. Ivanov, I. Bykov, G. Barbillon, K. Mochalov, D. Korzhov, A. Kovalev, A. Smyk, A. Shurygin, A. K. Sarychev, Plasmon localization and field enhancement in flexible metasurfaces, Phys. Rev. Appl. 22 (2024) 064064.
[56] G. Barbillon, J. -L. Bijeon, J. -S. Bouillard, J. Plain, M. Lamy de la Chapelle, P. -M. Adam, P. Royer, Detection in near-field domain of biomolecules adsorbed on a single metallic nanoparticle, J. Microsc. 229 (2008) 270–274.
[57] P. Leiderer, C. Bartels, J. König-Birk, M. Mosbacher, J. Boneberg, Imaging optical near-fields of nanostructures, Appl. Phys. Lett. 85 (2004) 5370–5372.
[58] A. Grubisic, E. Ringe, C. M. Cobley, Y. Xia, L. D. Marks, R. P. Van Duyne, D. J. Nesbitt, Femtosecond and picosecond near-field ablation of gold nanotriangles: nanostructuring and nanomelting, Appl. Phys. A 104 (2011) 793–799.
[59] K. Imura, H. Okamoto, M. K. Hossain, M. Kitajima, Visualization of localized intense optical fields in single gold-nanoparticle assemblies and ultrasensitive Raman active sites, Nano Lett. 6 (2006) 2173–2176.
[60] K. Ueno, S. Juodkazis, V. Mizeikis, K. Sasaki, H. Misawa, Clusters of closely spaced gold nanoparticles as a source of two-photon photoluminescence at visible wavelengths, Adv. Mater. 20 (2008) 26–30.
[61] K. Ueno, S. Juodkazis, T. Shibuya, Y. Yokota, V. Mizeikis, K. Sasaki, H. Misawa, Nanoparticle plasmon-assisted two-photon polymerization induced by incoherent excitation source, J. Am. Chem. Soc. 130 (2008) 6928–6929.
[62] T. Geldhauser, A. Kolloch, N. Murazawa, K. Ueno, J. Boneberg, P. Leiderer, E. Scheer, H. Misawa, Quantitative measurement of the near-field enhancement of nanostructures by two-photon polymerization, Langmuir 28 (2012) 9041–9046.
[63] L. Douillard, F. Charra, Z. Korczak, R. Bachelot, S. Kostcheev, G. Lerondel, P. -M. Adam, P. Royer, Short Range Plasmon Resonators Probed by Photoemission Electron Microscopy, Nano Lett. 8 (2008) 935–940.
[64] C. Awada, J. Plathier, C. Dab, F. Charra, L. Douillard, A. Ruediger, High resolution scanning near field mapping of enhancement on SERS substrates: comparison with photoemission electron microscopy, Phys. Chem. Chem. Phys. 18 (2016) 9405–9411.
[65] M. Dabrowski, Y. Dai, H. Petek, Ultrafast Photoemission Electron Microscopy: Imaging Plasmons in Space and Time, Chem. Rev. 120 (2020) 6247–6287.
[66] M. Hardy, P. Goldberg Oppenheimer, 'When is a hotspot a good nanospot' – review of analytical and hotspot-dominated surface enhanced Raman spectroscopy nanoplatforms, Nanoscale 16 (2024) 3293–3323.
[67] C. Awada, G. Barbillon, F. Charra, L. Douillard, J. -J. Greffet, Experimental study of hot spots in gold/glass nanocomposite films by photoemission electron microscopy, Phys. Rev. B 85 (2012) 045438.
[68] P. Taugeron, M. Rahmani, N. Delorme, M. Faure, L. Douillard, J. -F. Bardeau, Quantitative PEEM and Raman Study of Nanorough Au SERS-Active Substrates for Molecular Sensing Applications, ACS Appl. Nano Mater. 6 (2023) 11135–11143.
[69] Y. Dai, M. Dabrowski, V. A. Apkarian, H. Petek, Ultrafast Microscopy of Spin-Momentum-Locked Surface Plasmon Polaritons, ACS Nano 12 (2018) 6588–6596.
[70] B. Ji, Q. Wang, X. Song, H. Tao, Y. Dou, X. Gao, Z. Hao, J. Lin, Disclosing dark mode of femtosecond plasmon with photoemission electron microscopy, J. Phys. D: Appl. Phys. 50 (2017) 415309.
[71] Q. Sun, K. Ueno, H. Yu, A. Kubo, Y. Matsuo, H. Misawa, Direct imaging of the near field and dynamics of surface plasmon resonance on gold nanostructures using photoemission electron microscopy, Light Sci. Appl. 2 (2013) e118.
[72] S. Mitiche, S. Marguet, F. Charra, L. Douillard, Plasmonics of regular shape particles, a simple group theory approach, Nano Res. 13 (2020) 1597–1603.
[73] P. Kahl, D. Podbiel, C. Schneider, A. Makris, S. Sindermann, C. Witt, D. Kilbane, M.H.-v. Hoegen, M. Aeschlimann, F. Meyer zu Heringdorf, Direct Observation of Surface Plasmon Polariton Propagation and Interference by Time–Resolved Imaging in Normal-Incidence Two Photon Photoemission Microscopy, Plasmonics 13 (2018) 239–246.
[74] A. Kubo, N. Pontius, H. Petek, Femtosecond Microscopy of Surface Plasmon Polariton Wave Packet Evolution at the Silver/Vacuum Interface, Nano Lett. 7 (2007) 470–475.
[75] D. Ramesh, B.G. Vijayakumar, T. Kannan, Therapeutic potential of uracil and its derivatives in countering pathogenic and physiological disorders, Eur. J. Med. Chem. 207 (2020) 112801.
[76] D. Zhu, Y. Wei, J. Yin, D. Liu, E.L. Ang, H. Zhao, Y. Zhang, A pathway for degradation of uracil to acetyl coenzyme A in bacillus megaterium, Appl. Environ. Microbiol. 86 (2020) 1–10.
[77] H.E. Krokan, F. Drabløs, G. Slupphaug, Uracil in DNA – occurrence, consequences and repair, Oncogene 21 (2002) 8935–8948.
[78] P. Rajapandiyan, J. Yang, Sensitive Cylindrical SERS Substrate Array for Rapid Microanalysis of Nucleobases, Anal. Chem. 84 (2012) 10277–10282.
[79] H. Xe, S. Zhu, P. Wen, D. Zhou, Y. Yin, Y. Lan, T. -C. Lee, Y. Zhang, Q. Pu, Raspberry-Like Plasmonic Nanoaggregates with Programmable Hierarchical Structures for Reproducible SERS Detection of Wastewater Pollutants and Biomarkers, Anal. Chem. 96 (2024) 17620–17630.
[80] G. Davison, T. Jones, J. Liu, J. Kim, Y. Yin, D. Kim, W. -I. K. Chio, I. P. Parkin, H. -H. Jeong, T. -C. Lee, Raspberry-Like Plasmonic Nanoaggregates with Programmable Hierarchical Structures for Reproducible SERS Detection of Wastewater Pollutants and Biomarkers, Adv. Mater. Technol. 8 (2023) 2201400.
[81] A. Dubey, R. Mishra, C. -W. Cheng, Y. -P. Kuang, S. Gwo, T. -J. Yen, Demonstration of a Superior Deep-UV Surface-Enhanced Resonance Raman Scattering (SERRS) Substrate and Single-Base MutationDetection in Oligonucleotides, J. Am. Chem. Soc. 143 (2021) 19282–19286.
[82] S. Almohammed, B. J. Rodriguez, J. H. Rice, Nucleobase sensing using highly-sensitive surface-enhanced Raman spectroscopy templates comprising organic semiconductor peptide nanotubes and metal nanoparticles, Sens. Bio-Sensing Res. 24 (2019) 100287.
[83] B. Giese, D. McNaughton, Surface-Enhanced Raman Spectroscopic Study of Uracil. The Influence of the Surface Substrate, Surface Poten-

tial, and pH, J. Phys. Chem. B 106 (2002) 1461–1470.
[84] K. -H. Cho, J. Choo, S. -W. Joo, Surface-enhanced Raman scattering and density functional theory calculation of uracil on gold and silver nanoparticle surfaces, Spectrochim. Acta Part A Mol. Biomol. Spectrosc. 61 (2005) 1141–1145.
[85] Z. -B. Lin, B. -G. Xie, J. -H. Tian, Y. -A. Tang, J. -J. Sun, G. -N. Chen, B. Ren, B. -W. Mao, Z. -Q. Tian, Potential-dependent adsorption of uracil on a silver electrode in alkaline solutions, J. Electroanal. Chem. 636 (2009) 74–79.
[86] M. Perez-Estebanez, W. Cheuquepan, J. V. Cuevas-Vicario, S. Hernandez, A. Heras, A. Colina, Double fingerprint characterization of uracil and 5-fluorouracil, Electrochim. Acta 388 (2021) 138615.
[87] R. Alvarez, J. M. García-Martín, M. Macías-Montero, L. González-García, J. C. González, V. Rico, J. Perlich, J. Cotrino, A. R. González-Elipe, A. Palmero, Growth regimes of porous gold thin films deposited by magnetron sputtering at oblique incidence: from compact to columnar microstructures, Nanotechnology 24 (2013) 045604.
[88] C. Humbert, O. Pluchery, E. Lacaze, A. Tadjeddine, B. Busson, Optical spectroscopy of functionalized gold nanoparticles assemblies as a function of the surface coverage, Gold Bull. 46 (2013) 299–309.
[89] L. Bossard-Giannesini, H. Cruguel, E. Lacaze, O. Pluchery, Plasmonic properties of gold nanoparticles on silicon substrates: Understanding Fano-like spectra observed in reflection, Appl. Phys. Lett. 109 (2016) 111901.
[90] R. Alvarez, A. Garcia-Valenzuela, G. Regodo, F. J. Ferrer, V. Rico, J. M. García-Martín, A. R. Gonzalez-Elipe, A. Palmero, Growth dynamics of nanocolumnar thin films deposited by magnetron sputtering at oblique angles, Nanotechnology 35 (2024) 095705.
[91] A. Das, K. Kumar, A. Dhawan, Periodic arrays of plasmonic crossed-bowtie nanostructures interspaced with plasmonic nanocrosses for highly sensitive LSPR based chemical and biological sensing, RSC Adv. 11 (2021) 8096–8106.
[92] V. M. Shalaev, A. K. Sarychev, Nonlinear optics of random metal-dielectric films, Phys. Rev. B 57 (1998) 13265.
[93] S. Ducourtieux, V. A. Podolskiy, S. Grésillon, S. Buil, B. Berini, P. Gadenne, A. C. Boccara, J. C. Rivoal, W. D. Bragg, K. Banerjee, V. P. Safanov, V. P. Drachev, Z. C. Ying, A. K. Sarychev, V. M. Shalaev, Near-field optical studies of semicontinuous metal films, Phys. Rev. B 64 (2001) 165403.
[94] D. Akolzina, V. G. Kravets, A. I. Berdyugin, A. N. Grigorenko, Optical Constants and Optical Anisotropy of Ultrathin Gold Films, Adv. Photonics Res. 5 (2024) 2300238.
[95] R. Schürmann, I. Bald, Decomposition of DNA Nucleobases by Laser Irradiation of Gold Nanoparticles Monitored by Surface-Enhanced Raman Scattering, J. Phys. Chem. C 120 (2016) 3001–3009.
[96] M.Cottat, N. Lidgi-Guigui, F. Hamouda, B. Bartenlian, D. Venkataraman, R. S. Marks, T. W. J. Steele, M. Lamy de la Chapelle, Highly sensitive detection of paclitaxel by surface-enhanced Raman scattering, J. Opt. 17 (2015) 114019.
[97] A. Tripathi, E. D. Emmons, N. D. Kline, S. D.Christesen, A. W. Fountain, J. A. Guicheteau, Molecular Structure and Solvent Factors Influencing SERS on Planar Gold Substrates, J. Phys. Chem. C 122 (2018) 10205–10216.
[98] E. D. Emmons, J. A. Guicheteau, A. W. Fountain, A. Tripathi, Effect of substituents on surface equilibria of thiophenols and isoquinolines on gold substrates studied using surface-enhanced Raman spectroscopy, Phys. Chem. Chem. Phys. 22 (2020) 15953–115965.
[99] G. Barbillon, O. Graniel, M. Bechelany, Assembled Au/ZnO Nano-Urchins for SERS Sensing of the Pesticide Thiram, Nanomaterials 11 (2021) 2174.
[100] A. Tripathi, E. D. Emmons, A. W. Fountain, J. A. Guicheteau, M. Moskovits, S. D. Christesen, Critical Role of Adsorption Equilibria on the Determination of Surface-Enhanced Raman Enhancement, ACS Nano 9 (2015) 584–593.
[101] Th. Dretschkow, A. S. Dakkouri, Th. Wandlowski, In-Situ Scanning Tunneling Microscopy Study of Uracil on Au(111) and Au(100), Langmuir 13 (1997) 2843–2856.
[102] R. A. Alvarez-Puebla, Effects of the Excitation Wavelength on the SERS Spectrum. J. Phys. Chem. Lett. 3 (2012) 857–866.
[103] D. -M. Tsai, C. -T. Lin, Fast normalized cross correlation for defect detection, Pattern Recognition Lett. 24 (2003) 2625–2631.
[104] R. Klette, P. Zamperoni, Handbook of Image Processing Operators, first ed., Wiley, 1996.